



Assessment of the Capability of Terahertz Time-Domain Spectroscopy as a Plasma Diagnostic

Nathan P. Brown¹ and Adam M. Steinberg²
Georgia Institute of Technology, Atlanta, GA, 30332, U.S.A.

Jason A. Deibel³
Wright State University, Dayton, OH, 45435, U.S.A.

Mitchell L. R. Walker⁴
Georgia Institute of Technology, Atlanta, GA, 30332, U.S.A.

Terahertz time-domain spectroscopy (THz-TDS) is a novel plasma diagnostic with the potential to augment the current suite of electric propulsion plasma diagnostic techniques. This work investigates the plasma diagnostic capabilities of THz-TDS with respect to: 1) measurable electron density and collision frequency, 2) the impact of boron nitride (BN) composite plasma boundaries, and 3) the impact of electron temperature and applied magnetic field. Assessment of the governing THz-TDS equations finds that the technique can resolve line-averaged electron densities ranging from $10^{13} - 10^{23} \text{ m}^{-3}$ and line-averaged electron collision frequencies ranging from $10^3 - 10^{12} \text{ Hz}$ in plasmas with a length of 1 m. THz-TDS is used to experimentally measure electron densities ranging from $1.4 - 3.0 \times 10^{19} \text{ m}^{-3}$ and electron collision frequencies ranging from $0.8 - 1.3 \times 10^{11} \text{ Hz}$ in an argon inductively coupled plasma (ICP) operating at 1 Torr and 60 – 200 W. Insertion of grade M26 BN in the THz pulse path is experimentally shown to cause deviation in measured electron density of less than or equal to $0.2 \times 10^{19} \text{ m}^{-3}$ ($\leq 7\%$) and deviation in measured electron collision frequency of less than or equal to $0.1 \times 10^{11} \text{ Hz}$ ($\leq 10\%$). Further analysis shows that, if the THz pulse propagates perpendicular to a magnetic field such that its polarization is aligned with the magnetic field, THz-TDS measurements are virtually independent of the magnetic field and are unaffected by electron temperatures as large as 10^4 eV .

I. Nomenclature

| | | |
|-----------|---|--|
| A | = | amplitude of the electric field spectrum transfer function |
| B | = | magnetic field strength |
| c | = | speed of light |
| E | = | electric field |
| \hat{E} | = | electric field spectrum |
| e | = | electron charge |
| FP | = | Fabry-Perot reflection term |
| i | = | the imaginary unit |

¹ Graduate Research Fellow, School of Aerospace Engineering, AIAA Student Member, nbrown44@gatech.edu

² Associate Professor, School of Aerospace Engineering, AIAA Associate Fellow

³ Associate Professor and Chair, Department of Physics

⁴ Professor and Associate Chair, School of Aerospace Engineering, AIAA Associate Fellow

| | | |
|-------------------|---|---|
| k_B | = | Boltzmann constant |
| L | = | plasma length |
| m_e | = | electron mass |
| n_e | = | electron density |
| \tilde{n} | = | complex refractive index |
| \tilde{n}_b | = | complex boron nitride refractive index |
| $\tilde{n}_{l,r}$ | = | complex plasma refractive index for pulse propagation along the magnetic field |
| \tilde{n}_p | = | complex plasma refractive index |
| \tilde{n}_\perp | = | complex plasma refractive index for pulse propagation perpendicular to the magnetic field |
| t | = | time |
| T_e | = | electron temperature |
| z | = | position in plasma along the pulse propagation direction |
| β | = | Faraday rotation angle |
| δt | = | temporal resolution of electric field |
| ϵ_0 | = | permittivity of free space |
| ν | = | electron collision frequency |
| τ | = | polarization ellipticity |
| Φ | = | phase of the electric field spectrum transfer function |
| ω | = | radiation frequency |
| ω_b | = | electron cyclotron frequency |
| ω_p | = | plasma frequency |

II. Introduction

Electric propulsion (EP) offers significant propellant mass savings compared to chemical propulsion, and, consequently, EP thrusters have become a mainstay technology for both satellite and space exploration vehicle propulsion [1]. Current research is engaged in improving well-established devices, such as Hall thrusters, understanding the physics limiting the performance of less mature devices, such as magnetoplasmadynamic thrusters, and developing novel thruster concepts, such as laser-plasma and Rotamak-type devices [2].

As each of these aims requires investigating the plasma physics that drive EP devices, plasma diagnostics are vital to EP research. Established electrostatic probe diagnostics, such as Langmuir, Faraday, retarding potential analyzer (RPA), and E×B probes, provide a wealth of plasma parameter information. However, electrostatic probes suffer ablation damage in high-density plasma conditions and can perturb plasma properties [3]. Recent work [4-7] has attempted to overcome these limitations through the development of noninvasive optical EP plasma diagnostics. Prominent examples include optical emission spectroscopy, laser-induced fluorescence, laser Thomson scattering, and microwave interferometry. Each technique carries its own set of strengths and limitations, and each is capable of resolving different plasma parameters in distinct conditions.

A novel technique that promises to augment the current suite of noninvasive optical EP plasma diagnostics is terahertz time-domain spectroscopy (THz-TDS) [8-18]. THz-TDS utilizes broadband pulsed THz radiation to measure line-integrated electron density and collision frequency. THz pulses can be focused and collimated to mm-scale diameters, and researchers [8,9,16] have demonstrated the ability of the technique to resolve plasma property evolution at ns and ps scales. The pulse frequency composition enables THz pulses to transmit through some visibly opaque dielectrics, such as boron nitride (BN) composites, and should enable a single THz-TDS setup to make measurements in a broad range of plasma conditions.

However, the range of plasma conditions in which THz-TDS can perform measurements has not yet been assessed. This paper analytically investigates THz-TDS capabilities with respect to: 1) measurable electron density and collision frequency, 2) the impact of BN composite plasma boundaries, and 3) the impact of electron temperature and applied magnetic field. The analysis is supported by experimental measurements made with the Georgia Tech High-Power Electric Propulsion Laboratory (HPEPL) THz-TDS system. Section III provides an overview of the HPEPL THz-TDS system, Section IV gives the governing THz-TDS equations, and Section V assesses THz-TDS capabilities.

III. HPEPL THz-TDS System

HPEPL houses a free-space THz-TDS system and tabletop inductively coupled plasma (ICP) discharge. The THz-TDS system generates THz radiation by optically pumping a BATOP PCA-60-05-10-800-h low temperature-grown

gallium arsenide (LT-GaAs) parallel-line photoconductive antenna (PCA) and electro-optically detects THz radiation by measuring the induced birefringence in a 1 mm-thick <110> zinc telluride (ZnTe) crystal. The optical table is electrically grounded and is actively vibration-isolated. Figure 1 shows a diagram of the THz-TDS system.

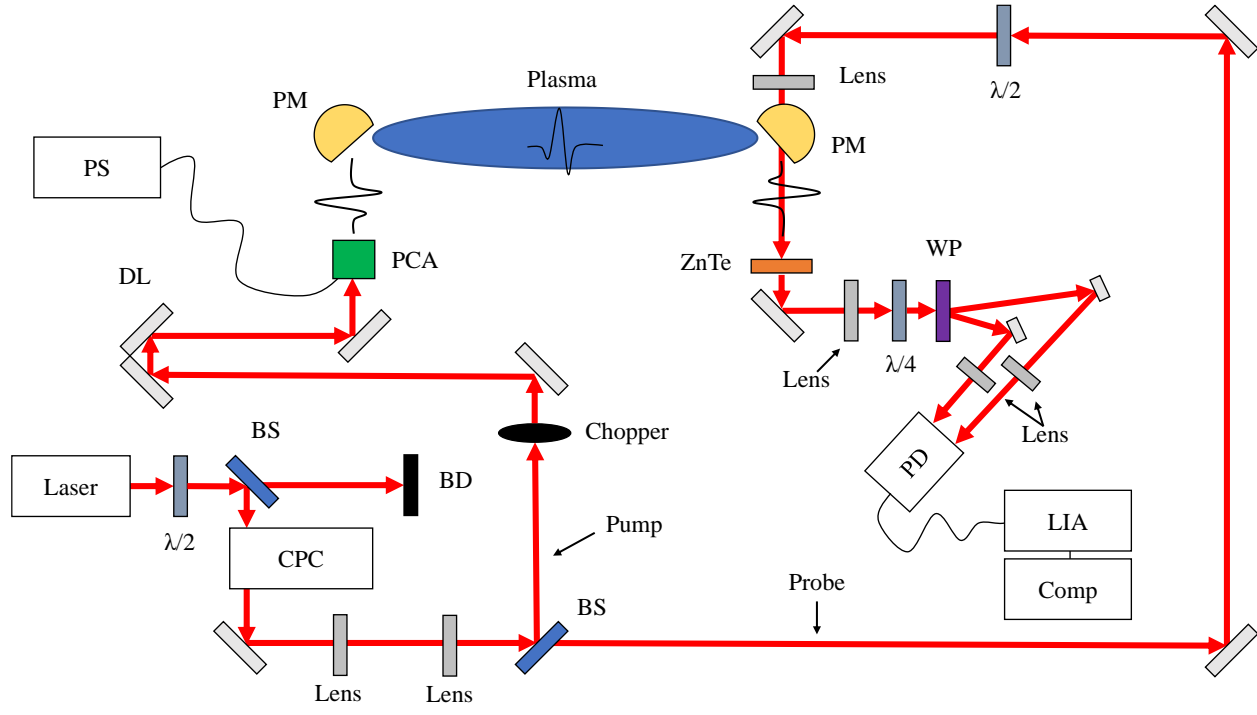


Fig. 1 Diagram of HPEPL THz-TDS system (BD: beam dump, BS: beam splitter, Comp: computer, CPC: pulse compressor, DL: delay line, LIA: lock-in amplifier, PCA: photoconductive antenna, PD: photodetector, PM: parabolic mirror, PS: power supply, WP: Wollaston prism, ZnTe: zinc telluride crystal, $\lambda/2$: half-wave plate, $\lambda/4$: quarter-wave plate).

A Coherent Vitora-T HP modelocked Ti:Sapphire laser generates ultrashort pulses with 800 nm center wavelength at a repetition rate of 100 MHz. Adjustable power input into the system is enabled by a rotatable half-wave plate and polarization-dependent beam splitter, and group velocity dispersion compensation is provided by a Coherent CPC II pulse compressor. Downstream of the pulse compressor, the beam is recollimated and then split into pump and probe paths.

The pump beam is routed through an optical chopper and variable delay line before it is focused onto the 5-micron PCA gap formed by gold electrodes patterned onto the LT-GaAs substrate. A DC voltage bias of 10 V is established across the PCA gap by an external power supply. Each ultrashort laser pulse has a full width at half maximum (FWHM) of approximately 50 fs and acts as a fast switch, generating photoelectrons in the gap that produce a transient current in response to the applied voltage bias [19]. The transient current radiates as a THz pulse that is coupled to air by a hyperhemispherical silicon lens and subsequently collimated and steered through the plasma discharge by a gold parabolic mirror. A second gold parabolic mirror focuses each THz pulse onto the ZnTe crystal, which is oriented so that the THz pulses propagate along the [110] axis with polarization parallel to the [1 1 0] axis.

The probe beam is focused onto the ZnTe crystal so that it copropagates through the crystal with the THz pulses at identical orientation and polarization. The THz pulses induce birefringence in the ZnTe, causing the originally linearly polarized probing laser beam to become elliptically polarized to a degree that is linearly proportional to the electric field strength of the THz pulses [20]. The ellipticity of the laser beam is measured with a quarter-wave plate, Wollaston prism, and balanced photodetector. Lock-in detection is provided by a Zurich Instruments MFLI lock-in amplifier (LIA) to extract the signal above noise. The LIA uses the 1 kHz optical chopper signal as a reference and is operated with a filter order of 3 and a time constant of 61 ms.

The electric field of each THz pulse spans many picoseconds, whereas the probing laser beam has a pulse FWHM of less than 50 fs. An entire THz pulse is resolved by temporally scanning the probing laser beam across the THz pulse in 50 fs increments. The HPEPL THz-TDS system accomplishes this by incrementally delaying the arrival of the THz pulses relative to the laser pulses with the variable delay line in the pump path. At each delay line position, 1000 samples are recorded after the LIA reaches its 99% settling time. The reported electric field at each delay line position is the average value across the 1000 samples. More details on the physics associated with THz generation and detection can be found in [18].

Plasma is generated by an argon radio frequency (RF) ICP discharge with a design similar to that of Ando et al. [13]. The discharge consists of a quartz tube cross (50 mm outer diameter, 3 mm wall thickness, 460 mm length, 250 mm width) connected to steel KF vacuum flanges by quick-connect couplings. A rotary-vane mechanical pump evacuates the discharge chamber to a base pressure of 1 mTorr, as measured by a convection pressure gauge (Kurt J. Lesker model KJL275807LL). Ultra-high purity (99.999%) argon is fed into the discharge by a regulator and precision flow meter. RF power is coupled to the plasma via a three-turn hollow copper antenna wrapped around the glass tube.

The unbalanced 13.56 MHz RF signal is generated by a Materials Science, Inc. RF-3-XIII power supply, tuned by a Palstar HF-AUTO antenna tuner, and converted to a balanced signal by a custom 1000 Ω current balun connected to the antenna. The plasma discharge is always operated with a standing wave ratio of 1.05 or lower. An electrically grounded Faraday cage surrounding the antenna prevents stray electromagnetic radiation or electrical arcs from interfering with THz-TDS system equipment.

The discharge viewports feature Z-cut crystalline quartz windows (Torr Scientific part BKVPZ50NQZ) that, compared to standard amorphous quartz windows, exhibit low THz absorption [21]. THz radiation is sent through the viewports and along the longer dimension of the quartz tube. Figure 2a shows the ICP discharge operating at 200 W and 1 Torr, and Fig. 2b shows the electric field of THz pulses measured with and without plasma. The pulses encompass resolvable frequencies ranging from approximately 0.3 to 2 THz. Section IV provides the governing equations used to extract plasma properties from measured THz pulses.

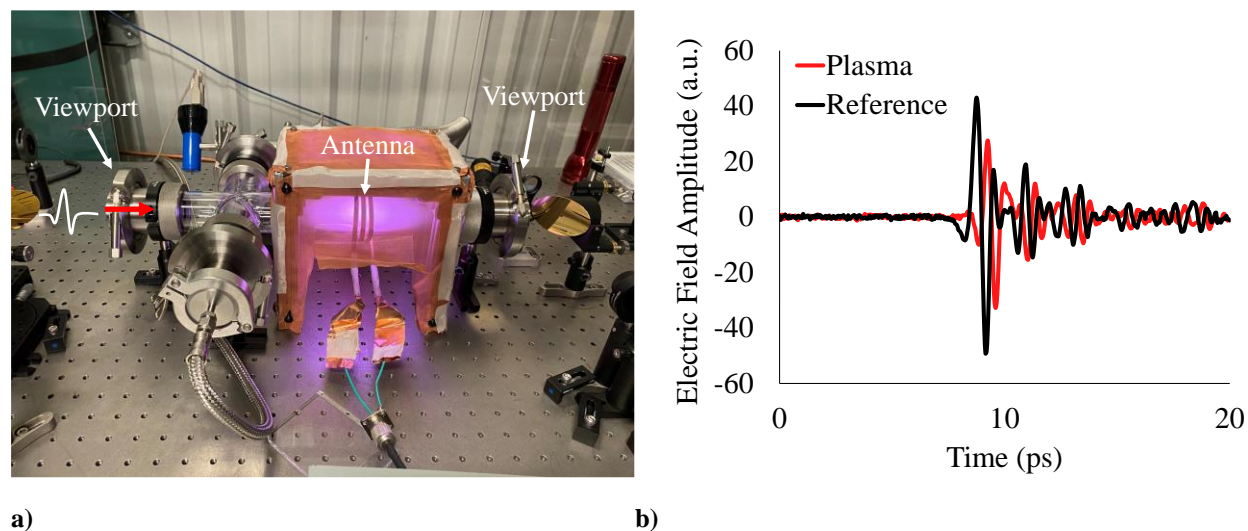


Fig. 2 a) radio frequency inductively coupled plasma discharge and b) THz pulses recorded with and without plasma (200 W, 1 Torr argon)

IV. Governing Equations

A. General Relations

THz-TDS measures the time-dependent electric field of a THz pulse with and without a sample in the THz pulse path [22,23]. The electric field measured with the sample in the pulse path is called the sample field and is denoted by $E_{sam}(t)$. The electric field measured without the sample in the pulse path is called the reference field and is denoted by $E_{ref}(t)$. Standard THz-TDS theory assumes the sample is bounded by vacuum for measurement of the sample pulse and replaced by vacuum for measurement of the reference pulse. In practice, however, the use of low-pressure air, nitrogen, or argon in place of vacuum produces negligible error [24].

The sample and reference fields are cast to the angular frequency (ω) domain by the discrete Fourier transform to determine the corresponding spectra, $\hat{E}_{sam}(\omega)$ and $\hat{E}_{ref}(\omega)$, respectively. Dividing the sample electric field spectrum by the reference electric field spectrum forms the transfer function

$$\frac{\hat{E}_{sam}(\omega)}{\hat{E}_{ref}(\omega)} = A(\omega) \exp[i\Phi(\omega)], \quad (1)$$

where A is the magnitude of the spectral ratio transfer function and Φ is its phase. These values, in turn, are related to the complex sample refractive index (\tilde{n}) by

$$A(\omega) = \exp \left[-\frac{\omega}{c} \int_0^L \text{Im}\{\tilde{n}(\omega, z)\} dz \right] \quad \text{and} \quad (2)$$

$$\Phi(\omega) = \frac{\omega}{c} \int_0^L [\text{Re}\{\tilde{n}(\omega, z)\} - 1] dz,$$

where c is the speed of light in vacuum, z is the position along the sample length, L is the total sample length, and $\text{Re}\{\}$ and $\text{Im}\{\}$ denote real and imaginary components, respectively. Equation (2) assumes the complex refractive index does not vary significantly on the scale of the radiation wavelength and thereby makes use of the Wentzel-Kramers-Brillouin (WKB) approximation.

B. Plasma Refractive Index

The plasma refractive index connects plasma properties to the measured sample and electric fields through Eqs. (1) and (2) [25-27]. Assuming electrons may be modeled as moving through a stationary fluid of ions and neutral particles, the interaction between electrons and other species may be approximated as viscous damping, the electron temperature and applied magnetic field are negligibly small, and the motion of a single electron is representative of the behavior of all electrons in the plasma, the complex plasma refractive index (\tilde{n}_p) is given by

$$\tilde{n}_p^2(\omega, z) = 1 - \frac{\omega_p^2(z)}{\omega[\omega + i\nu(z)]}, \quad (3)$$

where ν is the electron collision frequency and ω_p is the plasma frequency given as a function of electron number density (n_e), electron charge (e), electron mass (m_e), and the permittivity of free space (ϵ_0) by

$$\omega_p^2(z) = \frac{n_e(z)e^2}{\epsilon_0 m_e}. \quad (4)$$

Relaxation of the assumptions that the electron temperature and applied magnetic field are negligibly small produces a three-dimensional spatially dispersive system of equations with many solution regimes. However, this system may be simplified for two notable cases: 1) propagation of the THz pulse parallel to the magnetic field and 2) propagation of the THz pulse perpendicular to the magnetic field such that the pulse polarization is parallel to the magnetic field. The complex refractive index for case 1 is given by

$$\tilde{n}_{l,r}^2(\omega, z) = \left\{ 1 - \frac{\omega_p^2(z)}{\omega[\{\omega + iv(z)\} \pm \omega_b(z)]} \right\} / \left\{ 1 + \frac{\omega\omega_p^2(z)}{[\{\omega + iv(z)\} \pm \omega_b(z)]^3} \frac{k_B T_e(z)}{m_e c^2} \right\} \quad (5)$$

and the complex refractive index for case 2 is given by

$$\tilde{n}_{\perp}^2(\omega, z) = \left\{ 1 - \frac{\omega_p^2(z)}{\omega[\omega + iv(z)]} \right\} / \left\{ 1 + \frac{\omega\omega_p^2(z)}{[\omega + iv(z)][\{\omega + iv(z)\}^2 - \omega_b(z)]} \frac{k_B T_e(z)}{m_e c^2} \right\}, \quad (6)$$

where T_e is the electron temperature, k_B is the Boltzmann constant, and ω_b is the electron cyclotron frequency given as a function of the magnetic field strength (B) by

$$\omega_b = \frac{|e|B}{m_e}. \quad (7)$$

Eqs. (5) and (6) are valid if the electron temperature is below 100 keV [25,28]. The l and r subscripts in Eq. (5) refer to the left- and right-handed circular polarization components of the THz pulse and correspond to the + and - signs in the \pm sign, respectively. Here, the convention is that right-handed circular polarization refers to an electric field in which the y-component lags the x-component by a phase of $\pi/2$.

C. Common Simplifications

Use of Eq. (5) or Eq. (6) in conjunction with Eqs. (1) and (2) produces an indeterminate system unless measurements of the electron temperature and applied magnetic field are made with other instruments. Use of Eq. (3) with Eqs. (1) and (2) produces a closed system with a unique solution for the electron density and collision frequency. Substituting Eq. (3) into Eq. (2) results in

$$A(\omega) = \exp \left[-\frac{\omega}{c} \int_0^L \sqrt{-\frac{1}{2} \left(1 - \frac{\omega_p^2(z)}{\omega^2 + \nu^2(z)} \right) + \frac{1}{2} \sqrt{\left(1 - \frac{\omega_p^2(z)}{\omega^2 + \nu^2(z)} \right)^2 + \left(\frac{\omega_p^2(z)\nu(z)}{\omega[\omega^2 + \nu^2(z)]} \right)^2}} dz \right] \quad (8)$$

and

$$\Phi(\omega) = \frac{\omega}{c} \int_0^L \left[\sqrt{-\frac{1}{2} \left(1 - \frac{\omega_p^2(z)}{\omega^2 + \nu^2(z)} \right) + \frac{1}{2} \sqrt{\left(1 - \frac{\omega_p^2(z)}{\omega^2 + \nu^2(z)} \right)^2 + \left(\frac{\omega_p^2(z)\nu(z)}{\omega[\omega^2 + \nu^2(z)]} \right)^2}} - 1 \right] dz.$$

Determination of the electron density and collision frequency requires measurement of the sample and electric fields, calculation of the magnitude and phase of the spectral ratio, and numerical inversion of Eq. (8). However, for sufficiently low electron collision frequency, the electron density can be determined from the measured phase alone. Assuming $\nu \ll \omega_p$ and $\omega_p < \omega$ so that $\nu^2 \ll \omega^2 - \omega_p^2$, $\nu^2 \ll \omega^2(\omega^2 - \omega_p^2)^2/\omega_p^4$, and $\omega_p^2 \ll \omega^2$, the phase is related to the plasma frequency by

$$\Phi(\omega) = -\frac{1}{2\omega c} \int_0^L \omega_p^2(z) dz. \quad (9)$$

Use of the integral equations requires the assumption of plasma property distributions along the THz pulse path, determination of the plasma property distributions through a secondary measurement technique (such as optical emission spectroscopy), or determination of the plasma property distributions through additional THz-TDS measurements made along multiple beam paths. These complications can be avoided if the plasma is assumed uniform or if only line-integrated properties are required. In the uniform case, Eq. (8) simplifies to

$$A(\omega) = \exp \left[-\frac{\omega L}{c} \sqrt{-\frac{1}{2} \left(1 - \frac{\omega_p^2}{\omega^2 + \nu^2}\right) + \frac{1}{2} \sqrt{\left(1 - \frac{\omega_p^2}{\omega^2 + \nu^2}\right)^2 + \left(\frac{\omega_p^2 \nu}{\omega[\omega^2 + \nu^2]}\right)^2}} \right] \quad \text{and} \quad (10)$$

$$\Phi(\omega) = \frac{\omega L}{c} \left[\sqrt{\frac{1}{2} \left(1 - \frac{\omega_p^2}{\omega^2 + \nu^2}\right) + \frac{1}{2} \sqrt{\left(1 - \frac{\omega_p^2}{\omega^2 + \nu^2}\right)^2 + \left(\frac{\omega_p^2 \nu}{\omega[\omega^2 + \nu^2]}\right)^2}} - 1 \right],$$

and Eq. (9) simplifies to

$$n_e = -\Phi(\omega) \frac{2\epsilon_0 m_e c \omega}{e^2 L}. \quad (11)$$

Detailed derivations of the governing equations are provided in the appendix of a separate paper [18].

V. Capabilities Assessment

This section assesses THz-TDS measurement capabilities through analysis of the governing equations. Section V.A evaluates measurable electron density and collision frequency, Section V.B investigates the feasibility of measurements made in plasmas bounded and optically obscured by BN composite, and Section V.C determines the impact of electron temperature and magnetic field on THz-TDS measurements. Where possible, analyses are augmented by experimental measurements made by the HPEPL THz-TDS system.

A. Measurable Electron Density and Collision Frequency

1. General THz-TDS Capabilities

In the absence of large electron temperatures and magnetic fields, the line-averaged electron density and collision frequency are determined from the measured magnitude and phase of the spectral ratio transfer function through numerical inversion of Eq. (10). Electron density and collision frequency measurement capability is therefore driven by resolvable transfer function magnitude and phase. The maximum and minimum resolvable magnitudes at each frequency are a function of the system signal-to-noise ratio (SNR) and must be experimentally quantified. The minimum resolvable phase (Φ_{min}) at each frequency is given as a function of the temporal resolution (δt) of the THz field by

$$|\Phi_{min}(\omega)| = \omega\delta t. \quad (12)$$

Commercially available PCAs can collectively emit frequencies ranging from 0.01 to 5 THz with sufficient signal strength that total system magnitude SNR of at least 20:1 is readily achievable across this frequency range. THz pulse resolution of 10 fs is also achievable with commercially available equipment. Using these parameters as inputs, the full scope of measurable line-averaged electron densities and collision frequencies was calculated for various plasma lengths. Figure 3 shows the measurable parameter regions; yellow regions indicate measurable electron density and collision frequency, teal regions indicate measurable electron density only, and purple regions indicate that neither electron density nor collision frequency are measurable.

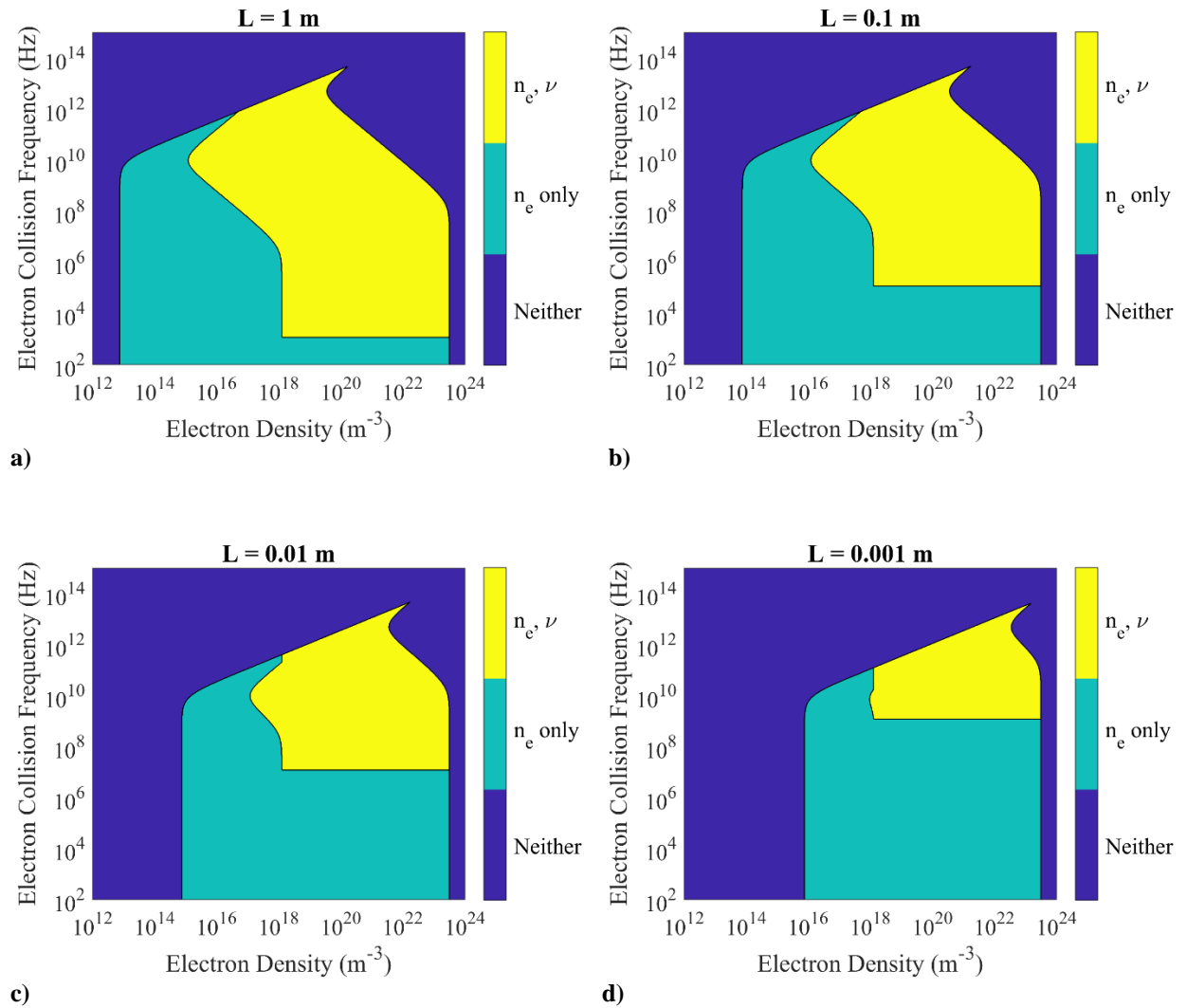


Fig. 3 Range of measurable line-averaged electron densities and collision frequencies by THz-TDS for plasma lengths of a) 1 m, b) 0.1 m, c) 0.01 m, and d) 0.001 m

Parameters are deemed “measurable” if, for any resolvable frequency, they produce resolvable changes in phase or phase and magnitude without attenuating that frequency beyond detectability. If only the change in phase is resolvable, only the electron density is measurable (with Eq. (11)). If both the phase and magnitude are resolvable, both the electron density and collision frequency are measurable. A resolvable phase is defined as a phase with magnitude greater than the minimum resolvable phase defined in Eq. (12). A resolvable magnitude is defined as a magnitude with a value that differs from unity by more than the magnitude SNR. A frequency component is deemed detectable if the magnitude at that frequency is greater than the magnitude SNR. For the assumed SNR of 20:1, resolvable magnitudes have values below 0.95 and detectable frequencies have magnitude values greater than 0.05. It should be noted that these definitions generate artificially sharp boundaries in detectable parameters. At these boundaries, measurement uncertainty approaches 100%.

Measurable electron densities and collision frequencies span many orders of magnitude. For a plasma length of 1 cm, measurable electron density ranges from approximately 10^{15} to 10^{23} m^{-3} and measurable electron collision frequency ranges from approximately 10^7 to 10^{12} Hz. However, the full range of measurable electron collision frequencies is only accessible if the electron density is within a relatively narrow band of values (10^{18} to 10^{22} m^{-3} in this case). Increasing plasma length enables lower plasma parameters to reshape the THz pulse and thereby decreases the lower measurable limits. For a plasma length of 1 m, for instance, the lowest measurable electron density becomes 10^{13} m^{-3} and the lowest measurable electron collision frequency becomes 10^3 Hz.

Upper limits on measurable electron density and collision frequency are enforced by plasma cut-off, conditions at which the plasma becomes highly reflective to probing radiation. In a collisionless plasma, cut-off occurs when the electron density is large enough that the plasma frequency becomes greater than or equal to a probing THz radiation frequency component. This effect is insensitive to plasma length. In a collisional plasma, however, the collision frequency may attenuate frequency components beyond the magnitude SNR at densities lower than the collisionless cut-off density. As can be seen in Fig. 3, this effect is exacerbated by longer plasma lengths for the same reason that longer plasma lengths permit measurement of lower plasma parameters.

Lower limits on measurable electron density and collision frequency are set by the temporal resolution of the THz electric field and the minimum resolvable THz radiation frequency and corresponding SNR. Measurement of lower electron collision frequencies can be achieved through the use of lower-frequency THz radiation components and the improvement of SNR. Measurement of lower electron density can be achieved through the use of lower-frequency THz radiation components and higher resolution of the THz electric field. Figure 4 shows the minimum resolvable electron density as a function of THz frequency and THz electric field resolution for collisionless plasma lengths of 0.01 m and 0.1 m. Utilizing lower THz frequencies and improving THz electric field resolution decreases the minimum resolvable electron density by orders of magnitude. The HPEPL THz-TDS system measures the THz electric field with a temporal resolution of 50 fs.

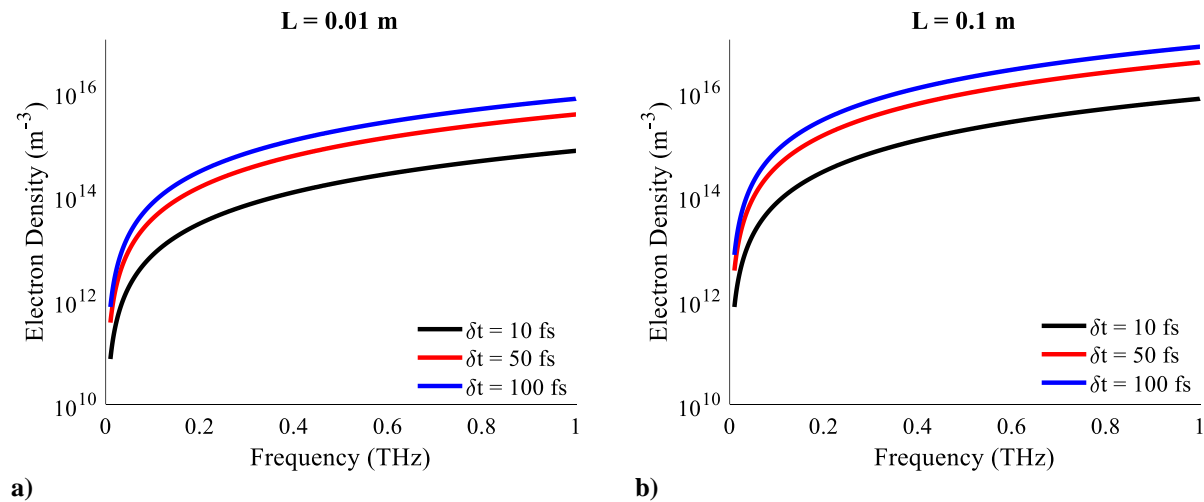


Fig. 4 Lower detectable line-averaged electron density limits for different THz pulse resolutions in collisionless plasma lengths of a) 0.01 m and b) 0.1 m

The assumption of a collisionless plasma enables the use of Eq. (11) in place of Eq. (10), eliminating the necessity to perform numerical inversion to determine the electron density. The error associated with this simplified electron density calculation was evaluated by calculating the spectral ratio transfer function magnitude and phase for a given electron density and collision frequency with Eq. (10), calculating the electron density from the calculated phase with Eq. (11), and comparing the result to the input electron density. Figure 5 shows the resulting error for a plasma length of 0.1 m and radiation frequencies of 0.1 and 1 THz. The error is lower than 5% for electron densities corresponding to plasma frequencies much lower than the radiation frequency and for electron collision frequencies much lower than the radiation frequency. However, error rises sharply as either the plasma frequency or electron collision frequency approaches the THz radiation frequency.

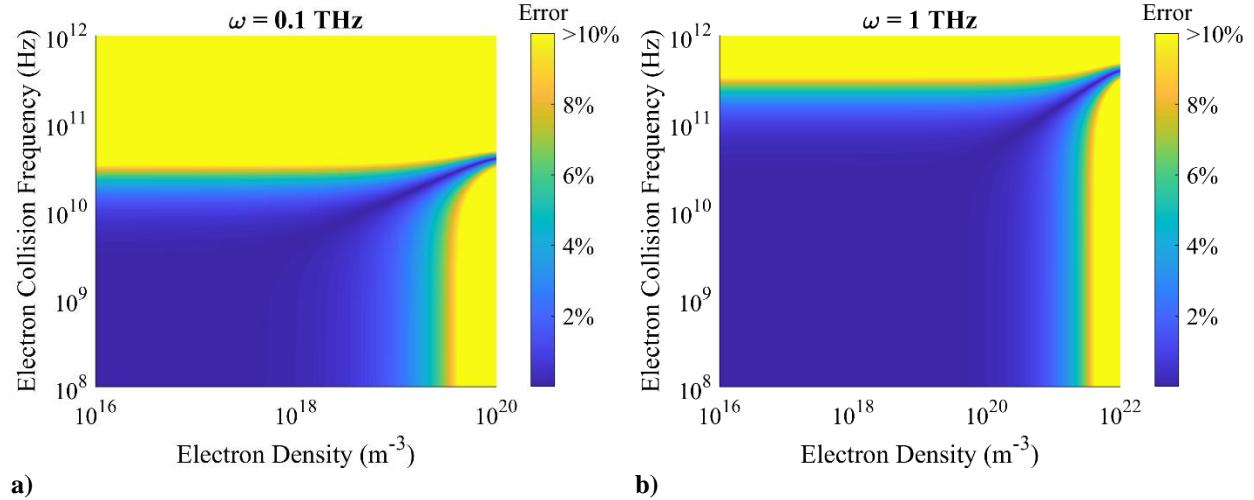


Fig. 5 Error associated with simplified line-averaged electron density calculation for a plasma length of 0.1 m for radiation with frequencies of a) 0.1 THz and b) 1 THz

2. HPEPL THz-TDS System Capabilities

The previous section detailed the general measurement capabilities of THz-TDS, under the assumption of the availability of the full scope of commercially available emission and detection methods. As noted in Section III, the HPEPL THz-TDS system presently resolves the THz electric field to 50 fs and can generate and detect THz frequencies ranging from approximately 0.3 to 2 THz. The phase resolution and magnitude SNR were experimentally quantified at all resolvable frequencies for determination of the line-averaged electron densities and collision frequencies measurable by the HPEPL THz-TDS system according to the criteria discussed in Section V.A.1. Figure 6 shows the measurable domains for a plasma length of 0.1 m. The plasma length of 0.1 m was chosen because, across the range of input powers discussed in this manuscript, the ICP discharge produces plasma lengths ranging from 10 to 14 cm.

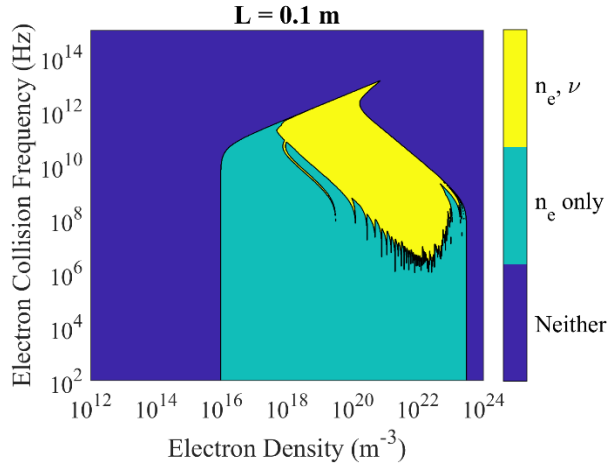


Fig. 6 Measurable line-averaged electron densities and collision frequencies by HPEPL THz-TDS system for a plasma length of 0.1 m

The HPEPL system is capable of resolving electron densities ranging from 10^{16} to 10^{23} m^{-3} and, depending on the electron density, electron collision frequencies ranging from 10^7 to 10^{12} Hz. The most notable differences between Fig. 6 and Fig. 4b are the lower limits of the detectable electron density and collision frequency. The HPEPL system does not resolve the THz electric field with sufficiently high temporal resolution and does not utilize a PCA with sufficiently low frequency components to enable measurement of the lowest possible electron densities and collision frequencies. However, replacement of the present PCA with a lower-frequency component PCA would enable the system to more closely approach the lower parameter measurement capabilities of an ideal system.

Evidence of the HPEPL THz-TDS system measurement capability is given by Fig. 7, which shows line-averaged electron density and collision frequency calculated through inversion of Eq. (10) with the ICP discharge operating at 60 – 200 W and 1 Torr argon. Reported values are averages taken across all resolvable frequencies. Error is expected to be on the order of 10^{18} m^{-3} and 10^{10} Hz for the electron density and collision frequency measurements, respectively. Error bars are not reported because the accurate determination of error requires implementation of Bayesian statistical uncertainty quantification techniques.

At these conditions, the electron density is well within the system resolution capabilities and the electron collision frequency is near the resolution limit. The trend in electron density with increasing power matches that found by Ando et al. [13] with THz-TDS and Langmuir probe measurements in a similar ICP discharge operated under similar conditions. The plasma length at each power condition was determined through comparison of the plasma fluorescence with the known antenna outer diameter in high-resolution digital images.

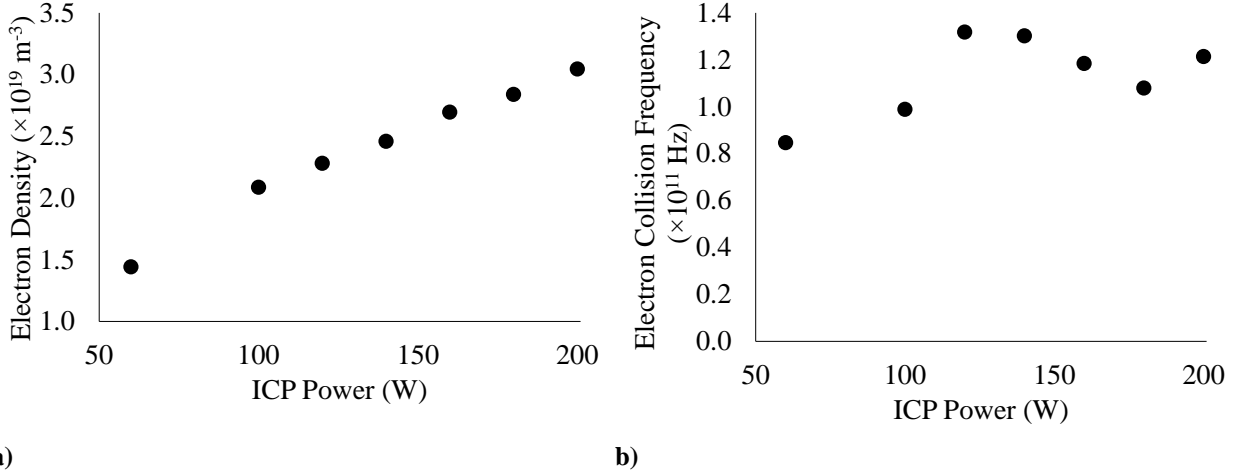


Fig. 7 HPEPL THz-TDS system measurements of line-averaged a) electron density and b) electron collision frequency in the ICP discharge (1 Torr argon)

B. Impact of BN Plasma Boundaries

1. Concept Overview

Of particular interest to the Hall thruster community is the capability to measure plasma parameters inside a Hall thruster discharge. However, noninvasive measurements of this region are challenging because the BN composite discharge walls and surrounding iron solenoids are opaque to most optical diagnostics. Hall thrusters that use four outer solenoids in a square pattern, rather than a single outer solenoid, permit discharge plasma access if the probing radiation can transmit through the BN walls.

Naftaly et al. [29] investigated the optical properties of various grades of BN with THz-TDS and found that BN exhibits some transparency to THz radiation. In a uniform plasma bounded by BN, the transfer function given in Eq. (1) must be modified to include non-vacuum boundaries and is given by

$$\frac{\hat{E}_{sam}(\omega)}{\hat{E}_{ref}(\omega)} = FP(\omega) \frac{4\tilde{n}_p(\omega)\tilde{n}_b(\omega)}{(\tilde{n}_p(\omega) + \tilde{n}_b(\omega))^2} \exp\left(i[\tilde{n}_p(\omega) - 1]\frac{\omega L}{c}\right), \quad (13)$$

where \tilde{n}_b is the BN complex refractive index and the $FP(\omega)$ term represents the impact of Fabry-Perot (FP) reflections inside the plasma [23]. FP reflections can be ignored, however, if the time required for the first reflected THz pulse to exit the plasma is less than the THz pulse duration. The required time to exit the plasma is given by

$$t = \frac{2L\text{Re}\{\tilde{n}_p(\omega)\}}{c}. \quad (14)$$

Because THz pulses are typically recorded for 10 – 100 ps, the minimum plasma thickness for which FP reflections can be ignored ranges from approximately 0.15 to 1.5 cm. THz-TDS may therefore be able to noninvasively measure plasma properties inside the Hall thruster discharge.

2. Plasma Measurements with BN in THz Pulse path

As a first test of the ability of THz-TDS to make measurements in plasmas optically obscured by BN composite, one $3 \times 2 \times 0.25$ in sample of grade M26 BN composite was placed in the THz pulse path. Grade M26 BN composite consists of 60% hexagonal close-packed BN and 40% amorphous silica by weight and closely resembles the wall material of many Hall thrusters [30]. The sample was oriented such that the THz radiation transmitted through the

0.25 in dimension and the polarization of the THz radiation was parallel to one of the ordinary axes of the orthotropic BN. Figure 8a shows the M26 BN placed in the THz radiation path, and Fig. 8b shows the resulting THz pulse electric fields recorded with and without plasma. In both images, the plasma was operated at 200 W and 1 Torr argon.

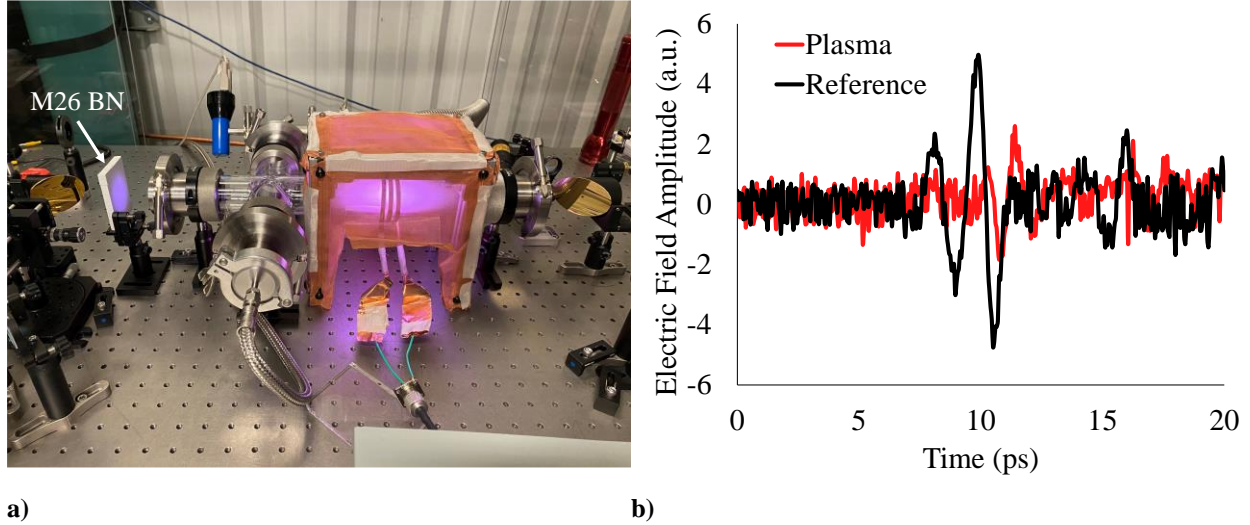


Fig. 8 a) measurement setup and b) measured THz pulse electric fields with M26 BN in the THz pulse path (200 W, 1 Torr argon)

Compared to the electric fields measured without M26 BN in the radiation path, the SNR is significantly diminished and the range resolvable frequencies is reduced to approximately 0.3 to 1 THz. However, determination of the electron density and collision frequency is still possible. Table 1 shows measurements of these values with the ICP discharge operating at 100 W and 200 W (1 Torr argon). The values were calculated with both Eq. (10) and Eq. (11) and are compared with measurements made without BN in the THz pulse path. Because the error is expected to be on the order of 10^{18} m^{-3} and 10^{10} Hz , for electron density and collision frequency, respectively, values are reported in Table 1 with two significant digits. An accurate error analysis requires Bayesian statistical uncertainty quantification techniques and will be the subject of future work.

Table 1 Comparison of plasma parameter measurements with and without M26 BN in THz pulse path

| | | 100 W | | 200 W | |
|----------|---------------------------------------|--------------|------------|--------------|------------|
| | | Unobstructed | BN in path | Unobstructed | BN in path |
| Eq. (11) | $n_e (\times 10^{19} \text{ m}^{-3})$ | 2.1 | 2.1 | 3.0 | 3.0 |
| Eq. (10) | $n_e (\times 10^{19} \text{ m}^{-3})$ | 2.1 | 2.2 | 3.0 | 3.2 |
| | $\nu (\times 10^{11} \text{ Hz})$ | 1.0 | 0.9 | 1.2 | 1.2 |

The electron densities calculated with the simplified Eq. (11) are equal to within two significant digits between obstructed and unobstructed measurements for both 100 W and 200 W. Use of Eq. (10) results in electron densities that differ by $0.1 - 0.2 \times 10^{19} \text{ m}^{-3}$ ($\leq 7\%$) and electron collision frequencies that differ by no more than $0.1 \times 10^{11} \text{ Hz}$ ($\leq 10\%$). The increase in the difference between calculated electron densities introduced by the use of Eq. (10) stems from the enhanced sensitivity of the electron density calculation to the spectral ratio transfer function magnitude SNR in Eq. (10) compared to Eq. (11).

These results indicate that the inclusion of M26 BN in the THz pulse path does not prevent plasma parameter measurement. Higher-fidelity measurements through greater lengths of BN will be made possible by increased THz electric field SNR.

C. Impact of Electron Temperature and Applied Magnetic Field

All measurements discussed and reported in Sections V.A and V.B use equations that neglect the impact of the electron temperature and applied magnetic field on the measured THz pulse electric field. Analysis of the impact of electron temperature and applied magnetic field effects are presented here for two specific cases: 1) propagation of the THz pulse parallel to the magnetic field and 2) propagation of the THz pulse perpendicular to the magnetic field such that the pulse polarization is parallel to the magnetic field.

1. Case 1: THz Pulse Propagation Parallel to Magnetic Field

Case 1 is most easily analyzed by decomposing the linearly polarized THz electric field into left- and right-handed circularly polarized components to enable the use of Eq. (5). If the attenuation is small enough that the THz electric field does not become significantly elliptically polarized, the impact of the magnetic field is to rotate the linearly polarized electric field by a Faraday rotation angle (β):

$$\beta(\omega) = \frac{1}{2} \frac{L\omega}{c} (\text{Re}\{\tilde{n}_l(\omega)\} - \text{Re}\{\tilde{n}_r(\omega)\}). \quad (15)$$

However, if one circularly polarized component is attenuated significantly more than another, the pulse will become elliptically polarized. The ellipticity (τ) of the polarization is quantified here as

$$\tau(\omega) = 100 \times \left(1 - \frac{\min[A_l(\omega), A_r(\omega)]}{\max[A_l(\omega), A_r(\omega)]} \right) \quad (16)$$

so that $\tau = 0$ corresponds to linear polarization and $\tau = 100$ corresponds to circular polarization. Because most THz-TDS systems can only measure linear polarization in one axis, Faraday rotation and pulse ellipticity produce errors in calculated plasma parameters.

Figure 9 shows the Faraday rotation angle and polarization ellipticity as a function of the electron temperature and applied magnetic field for an electron density of 10^{20} m^{-3} , electron collision frequency of 10^{11} Hz , uniform plasma length of 0.1 m, and probing radiation frequency of 1 THz. It is evident that pulse polarization is strongly affected by applied magnetic field strength and only weakly affected by the electron temperature. Under these conditions, magnetic field effects become important when the applied magnetic field approaches 1 T.

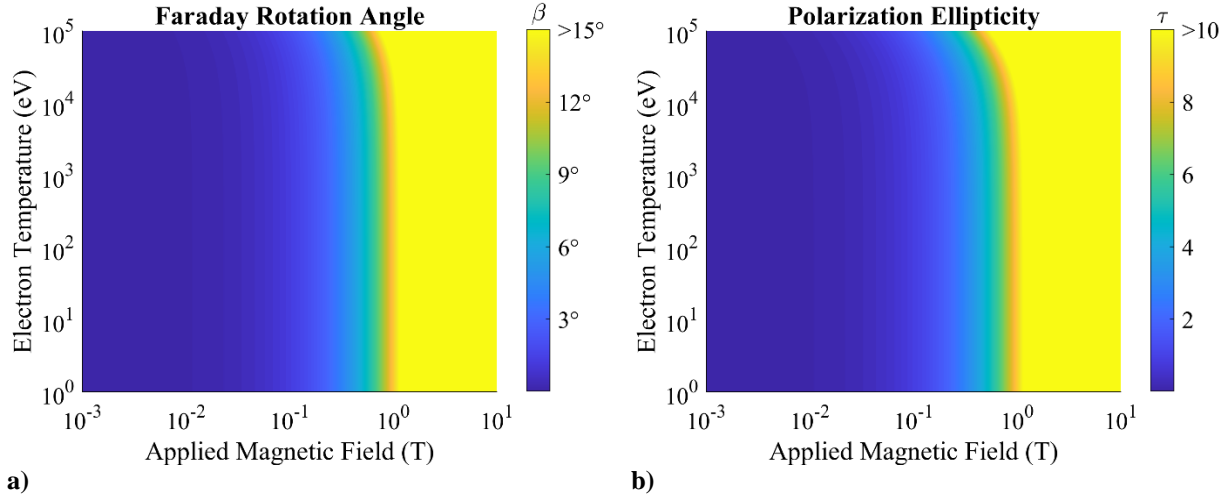


Fig. 9 Case 1 a) Faraday rotation angle and b) polarization ellipticity plotted as a function of electron temperature and applied magnetic field ($n_e = 10^{20} \text{ m}^{-3}$, $\nu = 10^{11} \text{ Hz}$, $\omega = 1 \text{ THz}$, $L = 0.1 \text{ m}$)

Figures 10, 11, and 12 show the Faraday rotation angle and polarization ellipticity as a function of the applied magnetic field and plasma length, electron density, and electron collision frequency, respectively. The plasma length and electron temperature are both approximately linearly related to the Faraday rotation angle and polarization ellipticity. For a given applied magnetic field, increasing these parameters increases the change in THz pulse polarization. Except at the largest electron collision frequencies, the Faraday rotation angle is relatively insensitive to electron collision frequency. However, polarization ellipticity grows approximately linearly with increasing electron collision frequency.

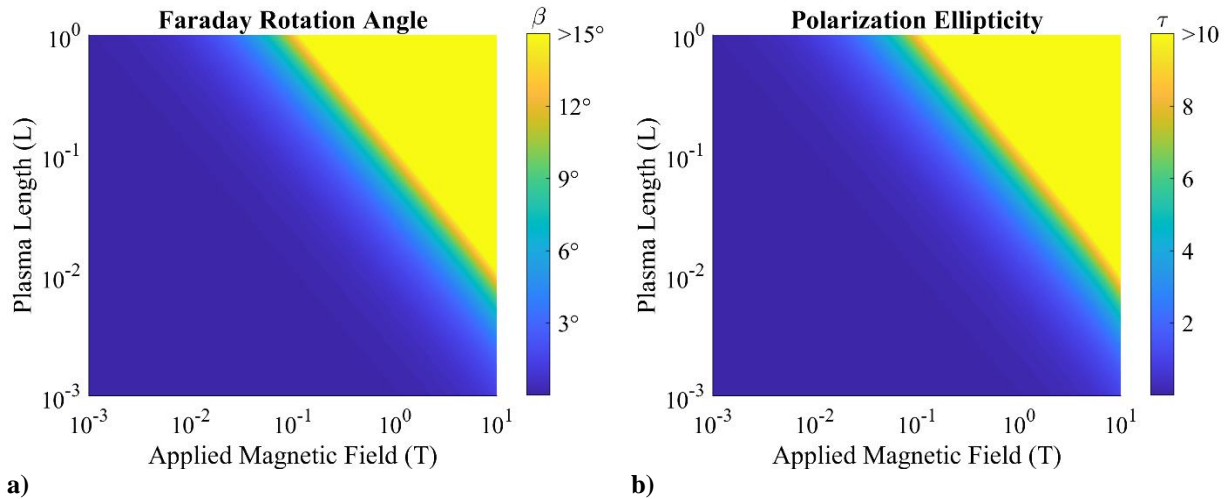


Fig. 10 Case 1 a) Faraday rotation angle and b) polarization ellipticity plotted as a function of plasma length and applied magnetic field ($T_e = 100 \text{ eV}$, $n_e = 10^{20} \text{ m}^{-3}$, $\nu = 10^{11} \text{ Hz}$, $\omega = 1 \text{ THz}$)

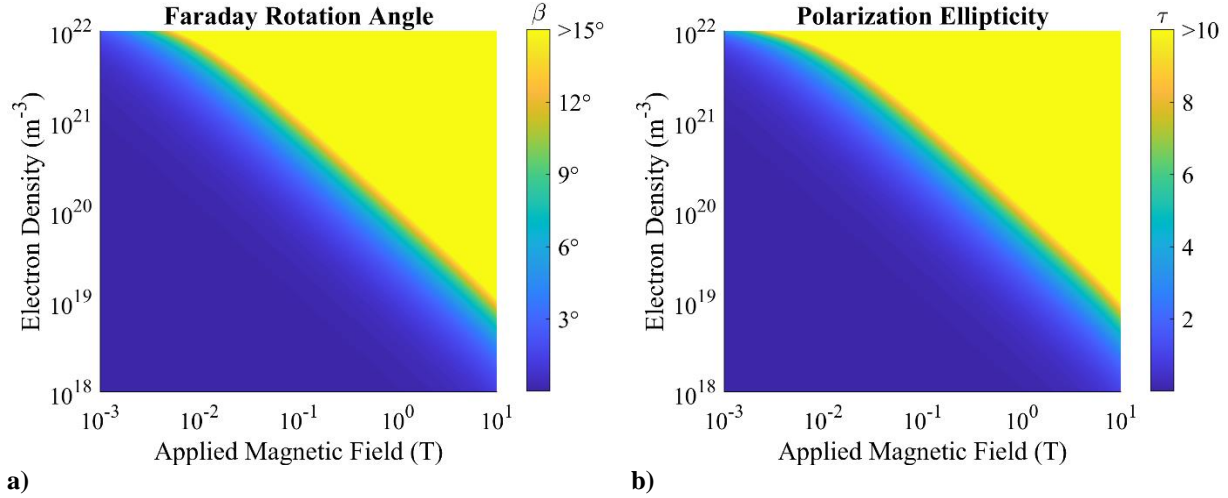


Fig. 11 Case 1 a) Faraday rotation angle and b) polarization ellipticity plotted as a function of electron density and applied magnetic field ($T_e = 100$ eV, $\nu = 10^{11}$ Hz, $\omega = 1$ THz, $L = 0.1$ m)

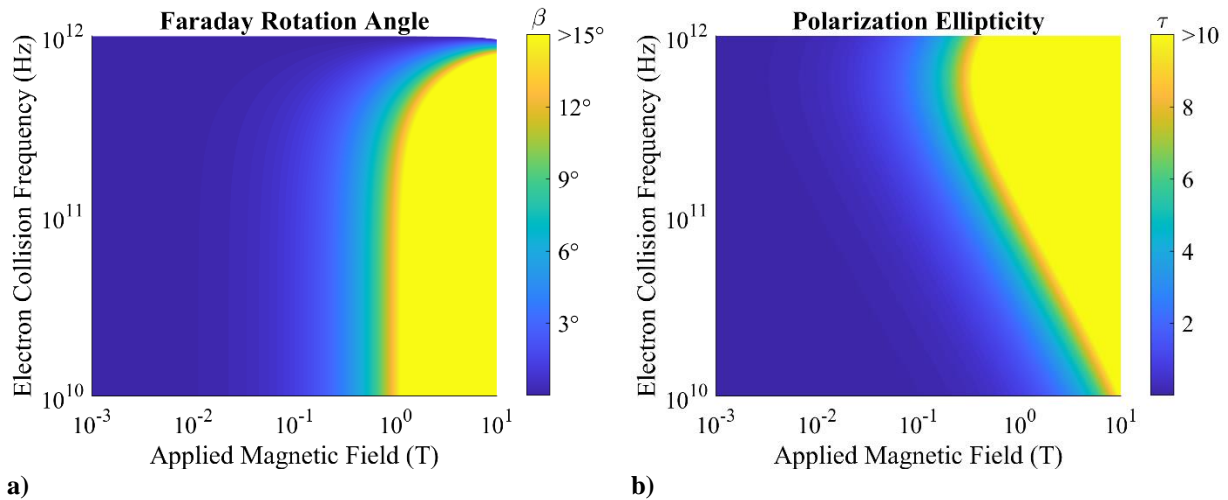


Fig. 12 Case 1 a) Faraday rotation angle and b) polarization ellipticity plotted as a function of electron collision frequency and applied magnetic field ($T_e = 100$ eV, $n_e = 10^{20} m^{-3}$, $\omega = 1$ THz, $L = 0.1$ m)

2. Case 2: THz Pulse Propagation Perpendicular to Magnetic Field with Polarization Parallel to Magnetic Field

THz pulse propagation in case 2 changes the transfer function magnitude and phase but does not impact pulse polarization. For analysis of the impact of case 2 propagation, the “measured” magnitude and phase of the spectral ratio were determined through direct calculation with Eq. (2) and Eq. (6) for an input electron density and collision frequency. Equation (10), which does not account for temperature or magnetic field effects, was then numerically inverted to extract the electron density and collision frequency associated with the measured magnitude and phase. The error associated with the failure to account for electron temperature and magnetic field was quantified as the percent difference between the input electron density and collision frequency and the extracted electron density and collision frequency.

Figure 13 shows the resulting calculation error in electron density and collision frequency as a function of the applied magnetic field and electron temperature for an electron density of $10^{20} m^{-3}$, electron collision frequency of

10^{11} Hz, uniform plasma length of 0.1 m, and probing radiation frequency of 1 THz. Contrary to case 1, the error in case 2 is strongly affected by the electron temperature and virtually independent of the applied magnetic field. The error becomes significant when the electron temperature reaches approximately 10^4 eV.

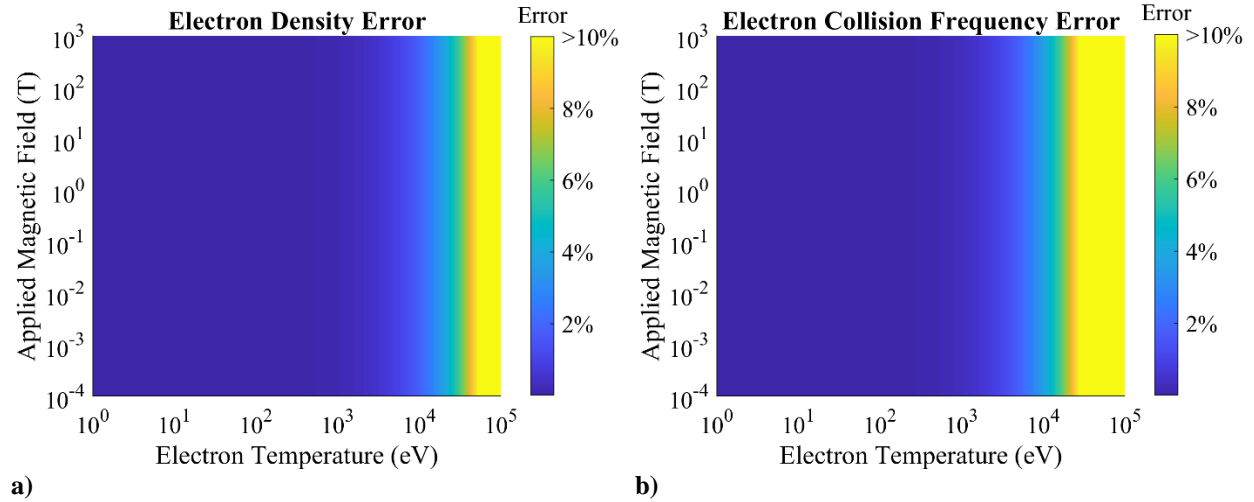


Fig. 13 Case 2 calculation error plotted as a function of applied magnetic field and electron temperature ($n_e = 10^{20} \text{ m}^{-3}$, $\nu = 10^{11} \text{ Hz}$, $\omega = 1 \text{ THz}$, $L = 0.1 \text{ m}$)

Figures 14, 15, and 16 show the electron density and collision frequency calculation error as a function of electron temperature and plasma length, electron density, and electron collision frequency, respectively. In each instance, the error is most strongly dependent on the electron temperature. The error becomes significant when the electron temperature reaches approximately 10^4 eV.

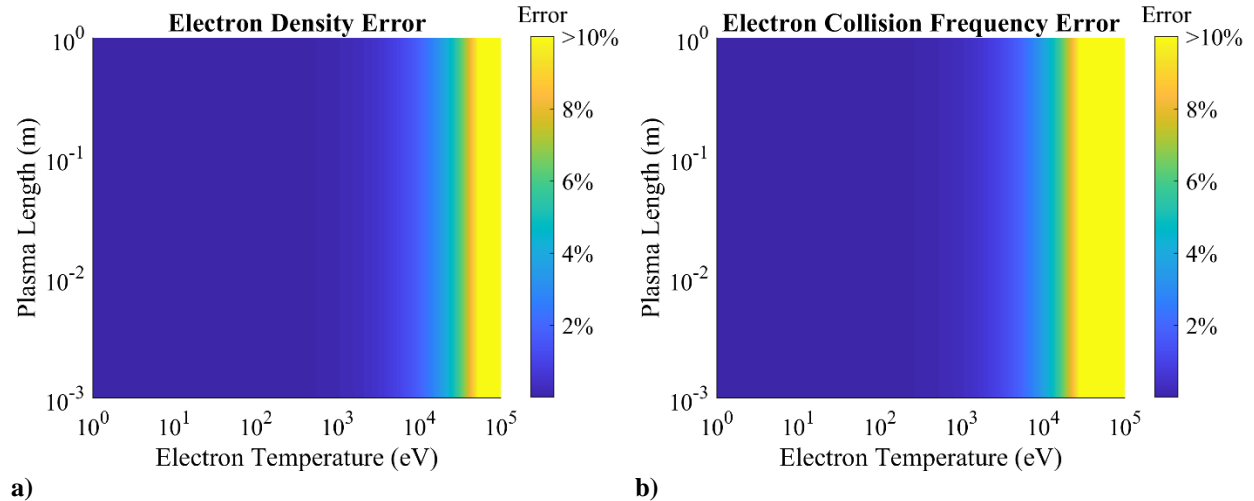


Fig. 14 Case 2 calculation error plotted as a function of plasma length and electron temperature ($B = 1 \text{ T}$, $n_e = 10^{20} \text{ m}^{-3}$, $\nu = 10^{11} \text{ Hz}$, $\omega = 1 \text{ THz}$)

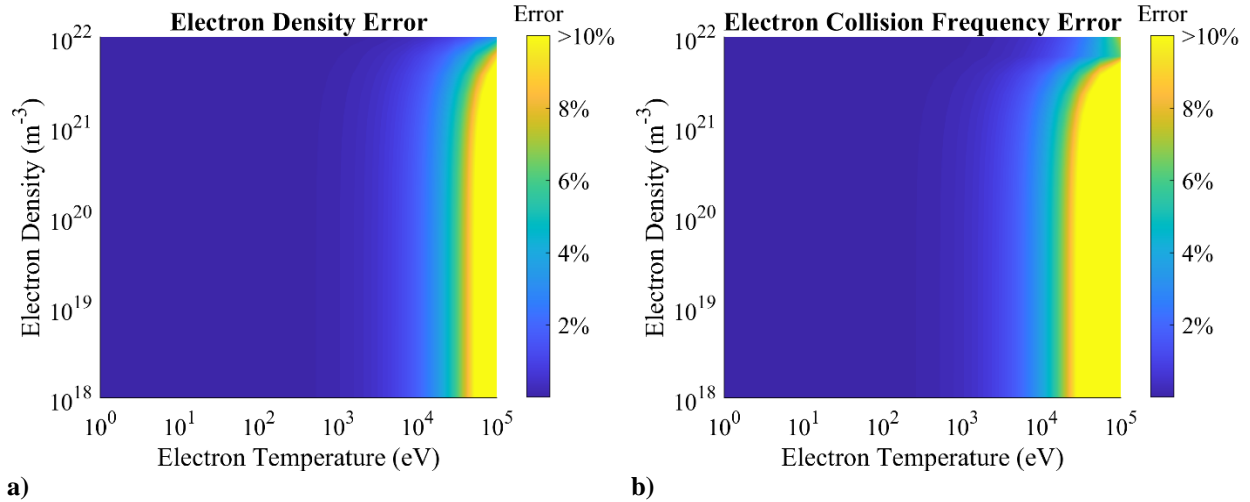


Fig. 15 Case 2 calculation error plotted as a function of electron density and electron temperature ($B = 1$ T, $\nu = 10^{11}$ Hz, $\omega = 1$ THz, $L = 0.1$ m)

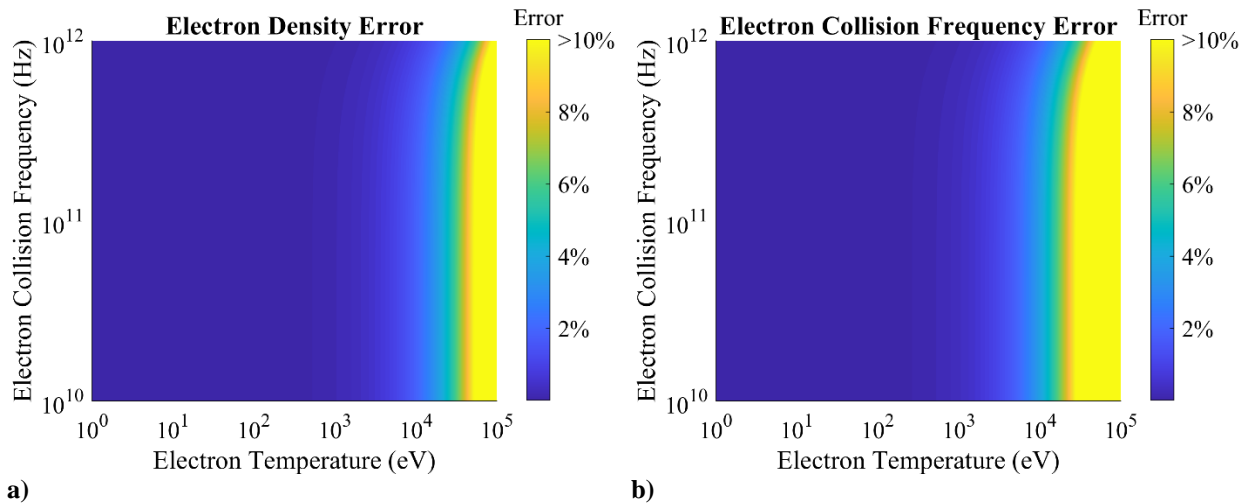


Fig. 16 Case 2 calculation error plotted as a function of electron collision frequency and electron temperature ($B = 1$ T, $n_e = 10^{20}$ m $^{-3}$, $\omega = 1$ THz, $L = 0.1$ m)

VI. Conclusion

This work provides an investigation of the plasma diagnostic capabilities of THz-TDS with respect to measurable parameters, impact of BN composite boundaries, and impact of electron temperature and applied magnetic field. The broad range of frequencies accessible to THz-TDS makes it a suitable diagnostic technique for plasmas spanning a wide range of electron densities ($10^{13} - 10^{23}$ m $^{-3}$ in plasma length of 1 m) and collision frequencies ($10^3 - 10^{12}$ Hz in plasma length of 1 m). The demonstrated ability of THz-TDS to measure electron density and collision frequency in plasma obscured by BN composite makes it a candidate for use in internal Hall thruster plasma diagnostics. If the THz pulse propagates perpendicular to the magnetic field such that its polarization is aligned with the magnetic field, THz-TDS can make measurements in plasmas with high electron temperatures ($\sim 10^4$ eV) and arbitrarily large applied magnetic fields. These characteristics suggest that THz-TDS is a promising diagnostic that may enable investigation of presently inaccessible electric propulsion plasma phenomena.

Acknowledgments

Nathan Brown is supported by the National Science Foundation Graduate Research Fellowship under grant number DGE-1650044, an Achievement Reward for College Scientists sponsored by Siemens, and the Georgia Tech Institute for Materials Graduate Student Fellowship. The authors thank Wyatt Amacker for his helpful assistance with data acquisition.

References

- [1] Lev, D., Myers, R. M., Lemmer, K. M., Kolbeck, J., Koizumi, H., and Polzin, K., "The technological and commercial expansion of electric propulsion," *Acta Astronautica*, Vol. 159, 2019, pp. 213-227.
doi: 10.1016/j.actaastro.2019.03.058
- [2] Levchenko, I., Xu, S., Mazouffre, S., Lev, D., Pedrini, D., Goebel, D., Garrigues, L., Taccogna, F., and Bazaka, K., "Perspectives, frontiers, and new horizons for plasma-based space electric propulsion," *Physics of Plasmas*, Vol. 27, No. 2, 2020, Paper 020601.
doi: 10.1063/1.5109141
- [3] Hutchinson, I. H., *Principles of Plasma Diagnostics*, Cambridge University Press, New York, 2002.
- [4] Mazouffre, S., "Laser-induced fluorescence diagnostics of the cross-field discharge of Hall thrusters," *Plasma Sources Science and Technology*, Vol. 22, No. 1, 2013, Paper 013001.
doi: 10.1088/0963-0252/22/1/013001
- [5] Dedrick, J. P., Gibson, A. R., Rafalskyi, D., and Aanesland, A., "Phase-resolved optical emission spectroscopy of a neutralizer-free gridded ion thruster," *International Electric Propulsion Conference*, Electric Rocket Propulsion Society (ERPS), IEPC Paper 2017-330, Atlanta, GA, USA, 2017.
- [6] Friss, A. J., and Yalin, A. P., "Cavity-enhanced Thomson scattering measurements of electron density and temperature in a hollow cathode discharge," *Optics Letters*, Vol. 43, No. 21, 2018, pp. 5343-5346.
doi: 10.1364/OL.43.005343
- [7] Vincent, B., Tsikata, S., Mazouffre, S., and Boniface, C., "Thomson scattering investigations of a low-power Hall thruster in standard and magnetically-shielded configurations," *36th International Electric Propulsion Conference*, Electric Rocket Propulsion Society (ERPS), IEPC Paper 2019-384, Vienna, Austria, 2019.
- [8] Jamison, S. P., Shen, J., Jones, D. R., Issac, R. C., Ersfeld, B., Clark, D., and Jaroszynski, D. A., "Plasma characterization with terahertz time-domain measurements," *Journal of Applied Physics*, Vol. 93, No. 7, 2003, pp. 4334-4336.
doi: 10.1063/1.1560564
- [9] Kolner, B. H., Conklin, P. M., Buckles, R. A., Fontaine, N. K., and Scott, R. P., "Time-resolved pulsed-plasma characterization using broadband terahertz pulses correlated with fluorescence imaging," *Applied Physics Letters*, Vol. 87, No. 15, 2005, Paper 151501.
doi: 10.1063/1.2103421
- [10] Ebbinghaus, S., Schröck, K., Schauer, J. C., Bründermann, E., Heyden, M., Schwaab, G., Böke, M., Winter, J., Tani, M., and Havenith, M., "Terahertz time-domain spectroscopy as a new tool for the characterization of dust forming plasmas," *Plasma Sources Science and Technology*, Vol. 15, No. 1, 2006, pp. 72-77.
doi: 10.1088/0963-0252/15/1/011
- [11] Mics, Z., Kadlec, F., Kužel, P., Jungwirth, P., Bradforth, S. E., and Apkarian, V. A., "Nonresonant ionization of oxygen molecules by femtosecond pulses: Plasma dynamics studied by time-resolved terahertz spectroscopy," *The Journal of Chemical Physics*, Vol. 123, No. 10, 2005, Paper 104310.
doi: 10.1063/1.2032987
- [12] Kolner, B. H., Buckles, R. A., Conklin, P. M., and Scott, R. P., "Plasma Characterization With Terahertz Pulses," *IEEE Journal of Selected Topics in Quantum Electronics*, Vol. 14, No. 2, 2008, pp. 505-512.
doi: 10.1109/JSTQE.2007.913395
- [13] Ando, A., Kurose, T., Reymond, V., Kitano, K., Kitahara, H., Takano, K., Tani, M., Hangyo, M., and Hamaguchi, S., "Electron density measurement of inductively coupled plasmas by terahertz time-domain spectroscopy (THz-TDS)," *Journal of Applied Physics*, Vol. 110, No. 7, 2011, Paper 073303.
doi: 10.1063/1.3633488
- [14] Jang, D., Uhm, H. S., Jang, D., Hur, M. S., and Suk, H., "Electron density characterization of inductively-coupled argon plasmas by the terahertz time-domain spectroscopy," *Plasma Sources Science and Technology*, Vol. 25, No. 6, 2016, Paper 065008.
doi: 10.1088/0963-0252/25/6/065008

- [15] Kang, K., Jang, D., and Suk, H., "Plasma density measurements using THz pulses from laser-plasmas," *Journal of Instrumentation*, Vol. 12, No. 11, 2017, Paper C11003.
doi: 10.1088/1748-0221/12/11/C11003
- [16] Meier, S. M., Tsankov, T. V., Luggenhölscher, D., and Czarnetzki, U., "Measurement of plasma densities by dual frequency multichannel boxcar THz time domain spectroscopy," *Journal of Physics D: Applied Physics*, Vol. 50, No. 24, 2017, Paper 245202.
doi: 10.1088/1361-6463/aa708f
- [17] Meier, S. M., Hecimovic, A., Tsankov, T. V., Luggenhölscher, D., and Czarnetzki, U., "First measurements of the temporal evolution of the plasma density in HiPIMS discharges using THz time domain spectroscopy," *Plasma Sources Science and Technology*, Vol. 27, No. 3, 2018, Paper 035006.
doi: 10.1088/1361-6595/aab188
- [18] Brown, N. P., Steinberg, A. M., Deibel, J. A., and Walker, M. L. R., "Terahertz Time-Domain Spectroscopy as an Electric Propulsion Plasma Diagnostic," *36th International Electric Propulsion Conference*, Electric Rocket Propulsion Society, IEPC Paper 2019-408, Vienna, Austria, 2019.
- [19] Auston, D. H., Cheung, K. P., and Smith, P. R., "Picosecond photoconducting Hertzian dipoles," *Applied Physics Letters*, Vol. 45, No. 3, 1984, pp. 284-286.
doi: 10.1063/1.95174
- [20] Wu, Q., and Zhang, X. C., "Free-space electro-optic sampling of terahertz beams," *Applied Physics Letters*, Vol. 67, No. 24, 1995, pp. 3523-3525.
doi: 10.1063/1.114909
- [21] Grischkowsky, D., Keiding, S., van Exter, M., and Fattinger, C., "Far-infrared time-domain spectroscopy with terahertz beams of dielectrics and semiconductors," *Journal of the Optical Society of America B*, Vol. 7, No. 10, 1990, pp. 2006-2015.
doi: 10.1364/JOSAB.7.002006
- [22] Withayachumnankul, W., and Naftaly, M., "Fundamentals of Measurement in Terahertz Time-Domain Spectroscopy," *Journal of Infrared, Millimeter, and Terahertz Waves*, Vol. 35, No. 8, 2014, pp. 610-637.
doi: 10.1007/s10762-013-0042-z
- [23] Duvillaret, L., Garet, F., and Coutaz, J., "A reliable method for extraction of material parameters in terahertz time-domain spectroscopy," *IEEE Journal of Selected Topics in Quantum Electronics*, Vol. 2, No. 3, 1996, pp. 739-746.
doi: 10.1109/2944.571775
- [24] Withayachumnankul, W., Fischer, B. M., Lin, H., and Abbott, D., "Uncertainty in terahertz time-domain spectroscopy measurement," *Journal of the Optical Society of America B*, Vol. 25, No. 6, 2008, pp. 1059-1072.
doi: 10.1364/JOSAB.25.001059
- [25] Heald, M. A., and Wharton, C. B., *Plasma Diagnostics with Microwaves*, John Wiley & Sons Inc., New York, 1965.
- [26] Stix, T. H., *Waves in Plasmas*, American Institute of Physics, New York, 1992.
- [27] Swanson, D. G., *Plasma Waves, 2nd ed.*, Insitute of Physics Publishing, Philadelphia, PA, 2003.
- [28] Yuan, C., Zhou, Z., Xiang, X., Sun, H., Wang, H., Xing, M., and Luo, Z., "Propagation properties of broadband terahertz pulses through a bounded magnetized thermal plasma," *Nuclear Instruments and Methods in Physics Research Section B: Beam Interactions with Materials and Atoms*, Vol. 269, No. 1, 2011, pp. 23-29.
doi: 10.1016/j.nimb.2010.10.003
- [29] Naftaly, M., and Leist, J., "Investigation of optical and structural properties of ceramic boron nitride by terahertz time-domain spectroscopy," *Applied Optics*, Vol. 52, No. 4, 2013, pp. B20-B25.
doi: 10.1364/AO.52.000B20
- [30] Brown, N. P., and Walker, M. L. R., "Review of Plasma-Induced Hall Thruster Erosion," *Applied Sciences*, Vol. 10, No. 11, 2020, Paper 3775.
doi: 10.3390/app10113775